Canadian Science Publishing | Canadian Journal of Civil Engineering

Investigating Low-Cost Rutting Assessments Using Low-Density Mobile LiDAR Data

Journal:	*Canadian Journal of Civil Engineering*
Manuscript ID	cjce-2025-0314.R2
Manuscript Type:	Research Article
Date Submitted by the Author:	29-Oct-2025
Complete List of Authors:	Faisal, Ali; The University of British Columbia, School of Engineering Gargoum, Suliman; University of British Columbia, School of Engineering
Is the manuscript for consideration in a Special Issue or Collection?:	Innovation, State of Practice, and Sustainability in Soils, Materials, and Pavement Engineering
Keyword:	Pavement Condition Assessment, Low-Cost LiDAR, Rutting, Deformation Analysis, Low Density LiDAR

SCHOLARONE™ Manuscripts

Investigating Low-Cost Rutting Assessments Using Low-Density Mobile LiDAR Data

Ali Faisal[a] and Suliman Gargoum[a]

[a]School of Engineering, University of British Columbia, British Columbia, Canada

ARTICLE HISTORY
Compiled December 17, 2025

ABSTRACT
Pavement rutting compromises driver safety, yet traditional inspections are slow and existing automated systems require expensive, high-resolution Light Detection and Ranging (LiDAR). This paper introduces a novel tile-based method to automatically quantify rutting using low-cost mobile LiDAR data. The algorithm identifies and measures ruts by modeling pavement deformations using computational geometry and surface fitting. A key contribution is a sensitivity analysis investigating the trade-off between point density and measurement accuracy. Tested on five road sections, the approach accurately measured rut depths as shallow as 3 mm. The analysis confirmed that low-density data, simulating low-cost sensors, can quantify ruts within practical error margins at a point density of 230 points per square meter (ppsm). The runtime for rutting estimation decreases from 83 to 34 seconds per kilometer when using low-density data. This study demonstrates a feasible and efficient solution for network-level rutting assessment, enabling wider and cost-effective adoption of LiDAR technology.

KEYWORDS
Pavement Condition Assessment; Low-Cost LiDAR; Rutting; Infrastructure Standardization; Deformation Analysis; Pavement Maintenance

1. Introduction

Permanent deformation, commonly known as rutting, is a critical issue that significantly impacts the performance of flexible pavements (Singh and Sahoo 2021). This issue appears as depressions or "channels" along the wheel path, caused by various factors related to the asphalt mixture, consolidation within the pavement layers, poor mix design, or viscoelastic flow of the asphalt, which are worsened by the repeated application of traffic loads. (Chilukwa and Lungu 2019). The development of ruts can severely affect road usability by diminishing skid resistance, heightening the chances of hydroplaning, and ultimately raising road maintenance expenses (Fwa *et al.* 2012). Regular road inspections and prompt maintenance are essential for making informed, timely, and cost-effective upkeep decisions. Such efforts are crucial for ensuring the safety of all road users.

Inspection methods are categorized into manual and automated techniques for pavement assessment and measurement. One common manual rut depth measurement method is ASTM's Standard E1703M-10 "Straight Edge" method (see Figures 1 and 2). It involves placing a straight-edge object on a lane covering the wheel path. The vertical distance between the edge and the bottom of the rut is then measured as illustrated in Figure 2. Other manual methods include the rod and level method. At the Long-Term Pavement Performance Program (LTPP) test tracks, the Dipstick Road Profiler was used for transverse profile measurements by taking the difference in elevation between incremental distances along the wheel path (Shtayat *et al.* 2020).

Although conventional methods provide accurate measurements of pavement distress, they are prone to human error, especially in harsh weather conditions. Fatigue and the inherent variability

CONTACT Ali Faisal Email: ali.faisal@ubc.ca

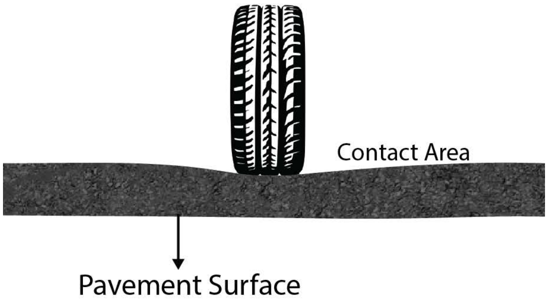

Figure 1.: Slightly deformed pavement along the wheel path

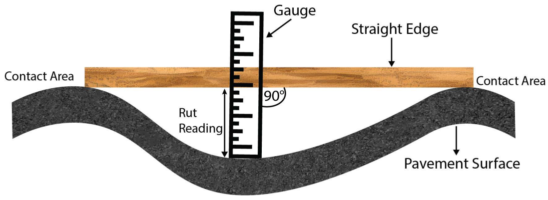

Figure 2.: ASTM's straight-edge method (ASTM 2023)

of human-operated equipment can further compromise field measurements. This is particularly true when similar assessments are repeatedly conducted on the same sections of road. Such methods become increasingly cumbersome when a network-level pavement assessment is required, especially when traffic disruptions are not feasible. Additionally, manual assessments can be labor-intensive, slow, and expose workers to various hazards on site (Serigos *et al.* 2012).

Automatic pavement assessment methods encompass a wide range of techniques and disciplines aimed at evaluating the rutting performance and rideability of roads. These methods include those that utilize image processing data, non-contact profilometers, and Mobile Light Detection and Ranging (LiDAR) technology. This paper focuses specifically on the latter.

LiDAR is a remote sensing technology that uses laser beams to generate high-resolution 3D maps of the scanned environment. The application of this technology for assessing various features of the road network has gained popularity in recent years (Gargoum *et al.* 2017, 2018a,b, Tripathi *et al.* 2023, Hatoum *et al.* 2023). The primary advantage of LiDAR over other assessment techniques is its ability to quickly capture a 3D representation of pavement surfaces over large areas at normal traffic speeds. LiDAR also offers richer 3D spatial coverage of the pavement surface when compared to other systems, such as laser profilers (Gargoum and El-Basyouny 2017). This capability is particularly useful for assessing pavement conditions at both network and project levels, allowing for continuous monitoring across vast areas while also identifying specific, localized distresses. Unlike profilers, LiDAR data is more cost-effective as it can be employed for additional applications, such as sight distance assessments and roadside asset inventories (Gargoum *et al.* 2017, 2018b). While some studies have utilized mobile LiDAR to assess pavement deformations (Faisal and Gargoum 2025b, Liu *et al.* 2022), they generally depend on expensive LiDAR sensors that provide more than 2000 points per square meter (ppsm). The operational costs of these sensors are significant, requiring substantial resources for both pre-processing and post-processing of data after collection. Also, using such systems for network-level surveys to evaluate only rutting is often impractical. Given this, the relationship between LiDAR point density and the accuracy of rutting assessments remains largely unexplored in the existing literature.

This paper presents a novel tile-based technique that uses LiDAR data to quantify and evaluate pavement rutting. The method moves beyond simple rut estimation to assess pavement rutting by analyzing the geometric 3D shape of ruts captured by LiDAR. Unlike existing methods, this approach does not depend on cross-sectional analysis to estimate rut depths. Moreover, it introduces an innovative assessment of the feasibility of using low-cost, low-density LiDAR for routine pavement rutting evaluations. Finally, this paper proposes an end-to-end solution that utilizes LiDAR datasets to evaluate rutting at various point density levels within a single scanning pass. To the best of the authors' knowledge, no study has yet explored the trade-off between LiDAR point density and rutting assessment feasibility.

2. Literature Review

Recent advancements in computer vision and machine learning have significantly streamlined pavement distress assessment, traditionally a tedious manual task. Techniques explored in recent literature include hybrid image-processing methods, regression-based modeling, and advanced deep neural networks (Arezoumand *et al.* 2021, Cao *et al.* 2021, Wang and Smadi 2011, Shatnawi *et al.* 2022, Ji *et al.* 2016, Ghosh and Smadi 2021).

The integration of LiDAR datasets into pavement assessment tasks has attracted growing attention due to their high-resolution data acquisition capabilities (Gargoum and El-Basyouny 2017). Regarding crack detection specifically, graph convolutional networks (GCNs), including variants employing saliency and dilated convolution techniques, have been successfully applied to analyze point cloud data (Feng *et al.* 2022, Ma and Li 2022). Alternative approaches involve converting 3D point clouds to 2D imagery and applying conventional image processing techniques for crack identification (Zhu *et al.* 2021, Xu and Yang 2019). Zhong et al. proposed a method where LiDAR point clouds are transformed into image formats using time grids, including scan angles and acquisition timestamps (Zhong *et al.* 2020). Georeferenced images derived from LiDAR data through inverse distance weighting were analyzed using tensor voting methods for crack extraction (Guan *et al.* 2015). Moreover, various filtering approaches based on elevation, intensity, and neighboring points in LiDAR data have also been proposed (Yongtao Yu *et al.* 2014, Phan and Huynh 2022).

However, compared to crack detection, methods for identifying pavement rutting directly from LiDAR data remain relatively unexplored. Famili et al. employed raster grid curvature metrics derived from point cloud data to detect rutting (Famili *et al.* 2021). El Issaoui et al. utilized Mobile Laser Scanning (MLS) data, identifying critical rut points via convex hull algorithms and k-means clustering, subsequently calculating rut depth against virtual reference surfaces (El Issaoui *et al.* 2021). Another study presented an approach identifying support points from rut profiles under constraints related to wheel path width and profile intersections (Firoozi Yeganeh *et al.* 2019). Gézero et al. proposed strategies for deriving transverse rut profiles from point clouds (Gézero and Antunes 2019). Shatnawi leveraged Canny edge detection applied to digital surface models generated from LiDAR to delineate wheel paths for cross-sectional rut depth analysis (Shatnawi *et al.* 2021). Additionally, Liu et al. generated various feature-based images from point clouds to analyze rut depths (Liu *et al.* 2022).

Despite achieving promising results, existing methodologies often face common limitations, such as heavy reliance on large annotated datasets, susceptibility to environmental conditions, and the computational burden of data processing (Tamagusko *et al.* 2024). Deep learning-based methods are heavily dependent on large annotated datasets for effective generalization to unseen scenarios (Shahrestani *et al.* 2024). In addition, external factors, such as varying lighting conditions and adverse weather, significantly compromise image quality and thus model reliability (Saha *et al.* 2022). Consequently, image-based annotations for pavement defects remain costly, time-intensive, and computationally demanding. Furthermore, traditional image data alone inadequately assesses rutting since elevation details are absent, necessitating advanced stereo-vision or 3D reconstruction techniques for precise deformation measurements (Dhiman and Klette 2020, Fan *et al.* 2020, Xu *et al.* 2023).

Research utilizing MLS data for rutting assessment remains limited, with existing studies predominantly relying on simplified cross-sectional data or involving complex transformations of point clouds, thereby underutilizing their inherent 3D spatial information. The precise positioning of cross-sections is critical, as it directly influences the accuracy of rut depth measurements and the subsequent analysis of distress severity. Overall, leveraging LiDAR-derived point clouds for pavement distress assessment presents substantial advantages, including detailed network coverage achievable at highway speeds, thereby minimizing traffic disruptions, safety hazards, and manual labor requirements. It's also worth noting that a single scan LiDAR dataset has broader applicability, including traffic sign recognition, highway asset inventory (e.g., traffic signals, guardrails, lane markings), sight distance measurement, geometric highway design, and autonomous vehicle support systems (Jung and Bae 2018, Gargoum and Gargoum 2024, Gargoum *et al.* 2018b, Gouda *et al.* 2023, Faisal and Gargoum 2025a, 2023-12-03). Furthermore, as evident from the literature review, another notable gap in current research involves the lack of studies exploring the trade-offs between point density of LiDAR data obtained from cost-effective sensors and the accuracy of rutting measurements.

To address the limitations in current literature, this study introduces an innovative methodology using single-pass mobile LiDAR data for detailed rutting assessment. This method directly analyzes pavement 3D features without the inefficient step of converting LiDAR data into secondary formats such as digital elevation models or image-based projections. The proposed solution enhances computational efficiency by simultaneously analyzing multiple pavement segments, accurately quantifying localized surface deformations, and flagging critical pavement conditions, thus offering significant improvements for practical, network-level assessments in industrial scenarios. Moreover, the paper specifically addresses the point density-accuracy trade-off gap by conducting a detailed sensitivity analysis to evaluate how variations in point cloud density impact the accuracy of rut depth measurements.

3. Data Acquisition and Preprocessing

The data analyzed in this study was collected by Nektar 3D Inc. along three roadway segments in Alberta, Canada. The selected routes include Highway 32, which spans from Swan Hills to the intersection at Highway 43, Township Road 510 (near Cawes Lake outside southeast Edmonton), and Miette Road, which branches off from Highway 16 close to Jasper National Park.

To gather the LiDAR datasets, the study utilized the Leica Pegasus: Two Ultimate Laser Scanning System (see Figure 3). This advanced platform consists of a GNSS receiver and an inertial measurement unit (IMU). It captures dense 3D point clouds while traveling at highway speeds, generating data points at a rate of up to one million per second with a relative accuracy of approximately 1 mm. The LiDAR technology employed is robust against varying road gradients, unlike traditional radar systems that can be affected by angle-of-incidence errors. The emitted laser pulses ensure comprehensive and detailed topographical coverage of the road surface. By combining LiDAR data with GNSS and IMU readings, the system accurately represents true road conditions while accounting for vehicle motion dynamics.

Synchronization between the LiDAR sensor and the GNSS/IMU system is achieved through a 200 Hz INS output rate. Although this frequency is lower compared to that of the LiDAR sensor, the high precision of the INS—with a gyro bias stability of 0.75 $\pm$ deg/hr and an accelerometer bias of 1 mg—ensures reliable data interpolation. Both sensor sets utilize GPS time to maintain synchronization. The system also incorporates dual antenna support and a robust wheel sensor that provides precise rotation pulses. These inputs are integrated using a Kalman filter to harmonize the differences in sensor data frequencies, ensuring an accurate representation of the vehicle's motion.

3.1. *LiDAR Data Preprocessing*

3.1.1. LiDAR Object Classification

A LiDAR scan includes a 3D representation of various structures such as buildings, vegetation, signage, and other roadside objects. To focus the analysis specifically on road surfaces, it is essential to segment these non-road points. Several advanced segmentation methods exist, including deep learning approaches such as PointNet++ (Qi *et al.* 2017), Kernel Point Convolution (KPConv) (Thomas *et al.* 2019), ConvPoint (Boulch 2020), and PointCNN (Li *et al.* 2018). The current study employs KPConv, a method that relies on kernel points rather than Multi-Layer Perceptrons (MLPs) to determine convolutional weights. During training, the model learns from labeled point clouds, minimizing prediction errors relative to known labels. At inference, this model classifies new data, effectively isolating the road surface from other scanned features.

3.1.2. *Point Cloud Noise Removal*

Point cloud noise, typically erroneous data points not representative of actual pavement surfaces, is eliminated using the k-nearest neighbor (KNN) algorithm. The method assesses each point based on its spatial proximity to surrounding points, removing isolated outliers. These outliers typically result from reflections off airborne particles or irrelevant objects. The computational efficiency and versatility of KNN, particularly its tunable 'k' parameter, make it especially suitable for handling extensive LiDAR datasets, effectively adapting to variations in point density.

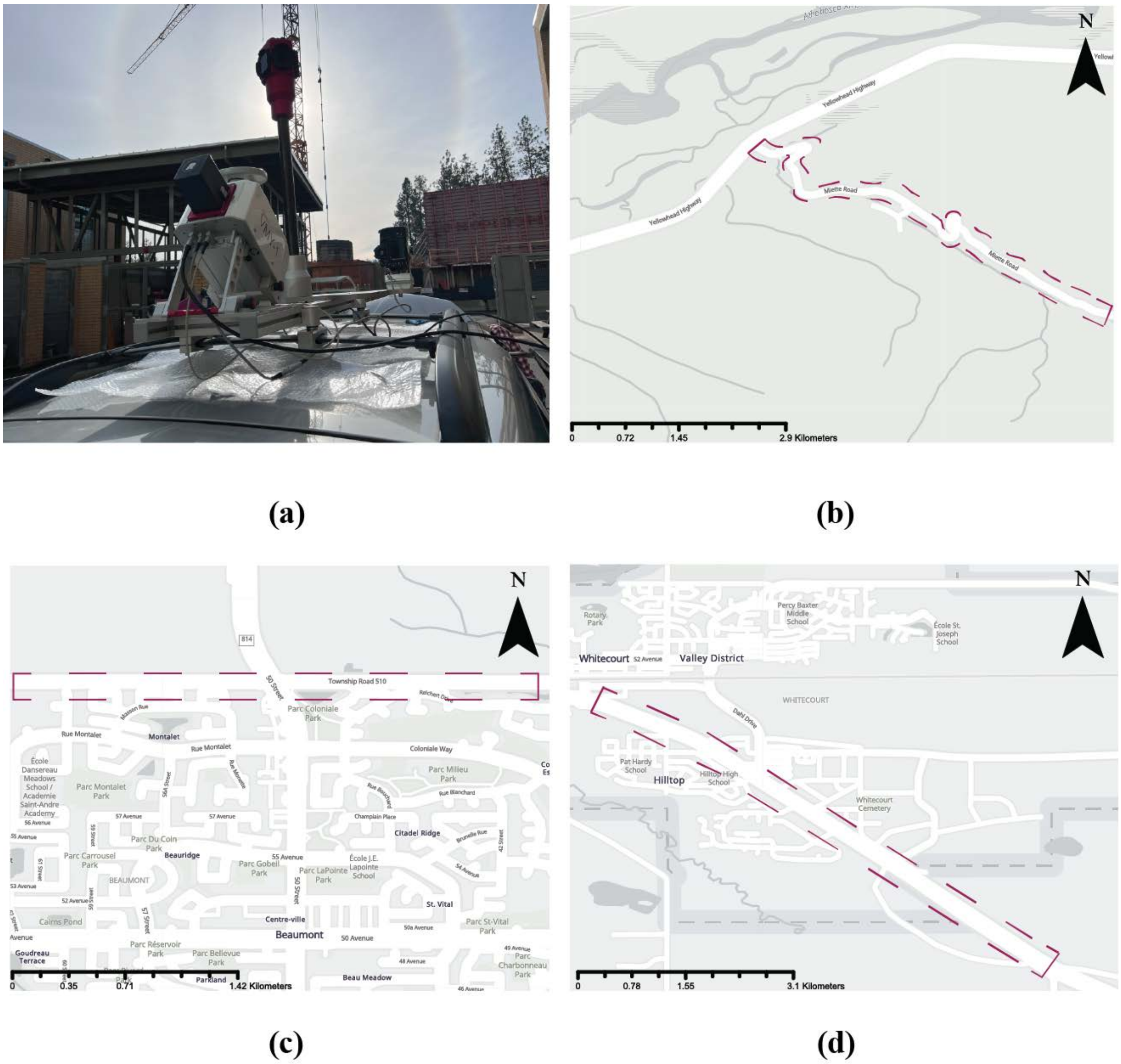

Figure 3.: Pavement point cloud data dataset acquisition: (a) Leica Pegasus Two Ultimate sensor, (b) Miette Road; (c) TW510 Road; (d) Highway 32 (Esri 2023).

3.2. *Point Cloud Data and Density*

MLS systems generate millions of data points, creating a detailed 3D representation of the environment known as a point cloud. These point clouds include not only road surfaces but also surrounding features such as vegetation, vehicles, pedestrians, and buildings. Point density, measured in points per square meter (*ppsm*), is a critical factor influencing the quality of those scans and the overall cost of the system. High-end systems like the Leica Pegasus: Two Ultimate can produce 1000-2000 *ppsm*, enabling the detection of fine details such as pavement defects. The Le-

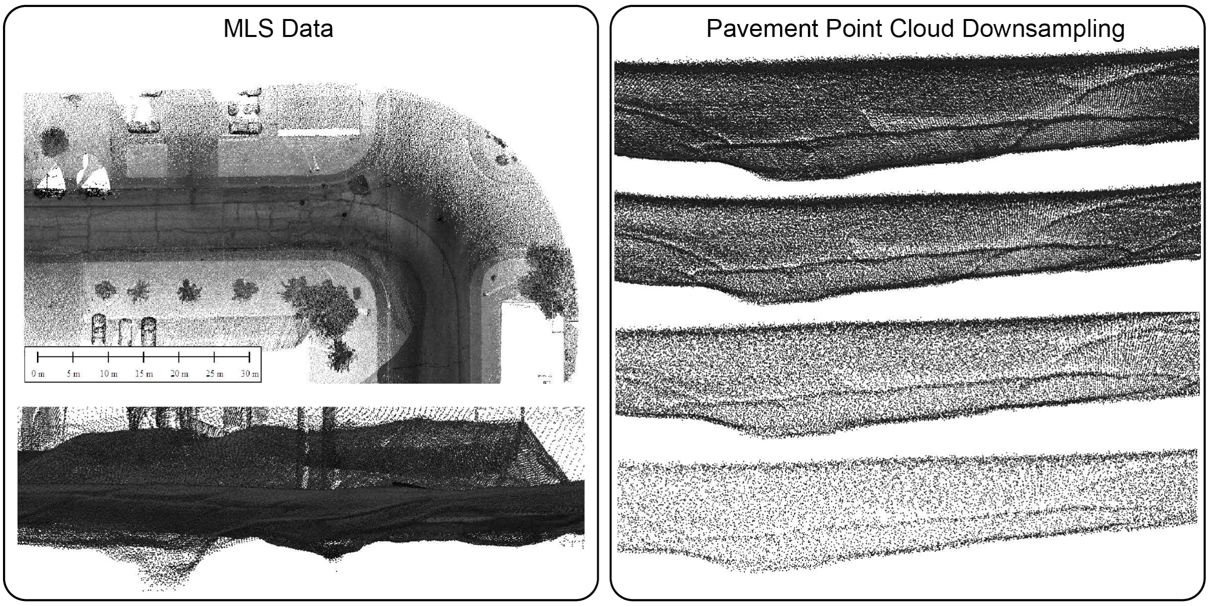

Figure 4.: Spatial thinning of LiDAR data.

ica Pegasus TRK 700 NEO typically achieves at least 1500 *ppsm*, while lower-end scanners may drop to around 200 *ppsm*. High-end systems can cost over $1 million, while lower-end scanners can be priced as low as $50,000.

3.2.1. Spatial Thinning Procedure

A spatial thinning procedure is employed on point cloud data to produce LiDAR datasets with differing point densities, as illustrated in Figure 4. A sample highway was selected to undergo spatial thinning for subsequent sensitivity analysis for rutting evaluations.

The data was downsampled using uniform spatial thinning across the entire dataset to retain the same data structure and distribution of point clouds. The process is deterministic and follows a fixed pattern where every N-th point from the dataset is retained. It can be represented in Equation 1, where P' is the subsampled set from the original point cloud P, and N is the interval at which points are retained. The point cloud dataset after spatial thinning is presented in Table 1:

$$P' = \{p_j \mid j \mod N = 0, \forall j \in \{1, 2, \ldots, m\}\} \tag{1}$$

Table 1.: Point cloud dataset after spatial thinning.

Dataset Description	**Point Count**	**Average ppsm**	**LiDAR Point Spacing (m)**
Highway 32			
High resolution	24,800,736	1280	0.0412
10% Reduction	22,320,664	1163.45	0.0435
25% Reduction	19,840,590	956.43	0.0461
33% Reduction	16,533,824	843.15	0.0506
50% Reduction	12,400,368	654.87	0.0584
75% Reduction	6,200,184	233.72	0.0825
90% Reduction	2,480,074	125.11	0.1312

The dataset underwent spatial thinning at six levels: 10%, 20%, 33%, 50%, 75%, and 90% of the original point cloud, as shown in Figure 4. Since uniform spatial thinning was used for downsampling, it is important to note that while the reduction in point cloud count directly corresponds to the reduction factor applied, this does not hold true for the resulting *ppsm* and point spacing. The *ppsm* is not directly proportional to the percentage of reduction due to the variable distribution of points across different elements of the scanned environment. In contrast, point spacing generally increases as the *ppsm* decreases, indicating a greater average distance between the remaining data points.

Specific reduction percentages were chosen to achieve a target *ppsm* on the pavement surface, simulating outputs from LiDAR sensors with varying scanning frequencies. The downsampling was carried out granularly because the original *ppsm* produced by the Leica Pegasus Two Ultimate System has a *ppsm* of 1000-2000. As a result, with a dense starting point, it is essential to gradually decrease point density to determine minimum detectable density thresholds for reliably triggering rutting failure modes.

Data collected from Highway 32, Miette Road, and TWP510 road using the Leica Pegasus Two Ultimate System were used to assess rutting. The goal was to validate whether the results obtained at higher resolutions would be comparable to those obtained from lower-density outputs of LiDAR sensors.

4. Methodology

The proposed algorithm involves several steps, including pavement surface extraction, preprocessing, boundary creation, tiling, plane fitting, and permanent deformation estimation. A summary of the proposed method is presented in Figure 5, and further detail about each step is provided in the following sections.

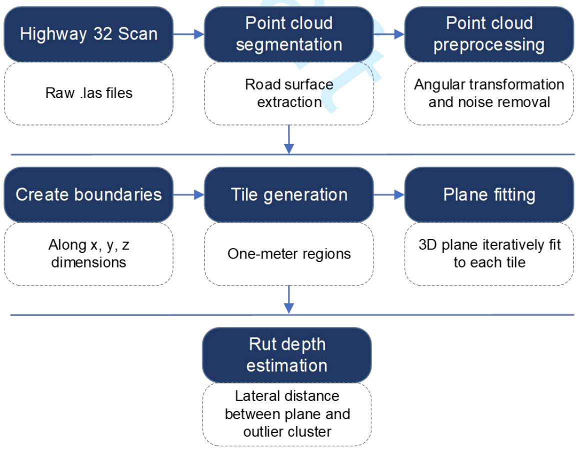

Figure 5.: Methodology flowchart.

Roads paved with asphalt are typically compacted to flatten the pavement surface and minimize lateral variations along the longitudinal direction. However, when rutting occurs, the surface is no longer flat because of the buildup of permanent deformations in the semi-viscous asphalt state, which is caused by issues related to the asphalt mix or consolidation of the base/subbase, which is exacerbated by repetitive loading. In the context of point clouds, when there is no deformation along the pavement, the surface is mostly flat, and the points belong to the same plane in 3D space. When rutting is present, point clouds reflect the spatial deformation that occurred along the pavement layer (see Figure 6). It can be observed that there is an abrupt change in the slope from the pavement to the rutting location, where the maximum value of deformation is located in the central lower region. Because rutting creates geometric irregularities, the planar features of a point cloud can be exploited to distinguish deformed areas from the surrounding flat pavement surface.

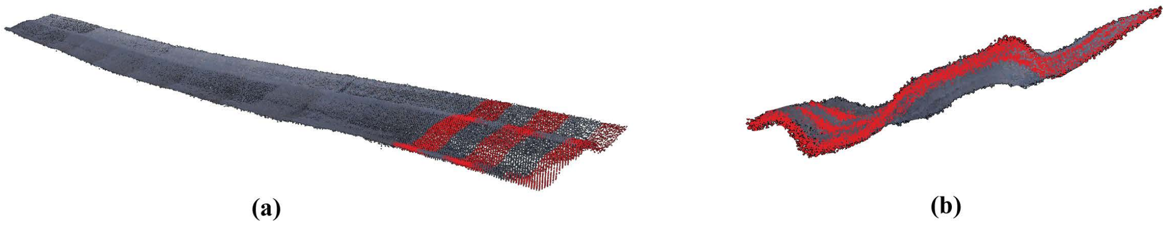

Figure 6.: Sample tiling of road surface point cloud with rutting along the wheel path: (a) linear road surface; (b) road cross-section.

4.1. *Road Surface Extraction*

After classifying the LiDAR scan into various categories of highway assets and environmental features, the road surface (pavement point cloud) is segmented out as shown in Figure 6a. Rotational and angular adjustments are made with respect to the centerline of the road, which involves aligning the orientation of the LiDAR data with the direction of the road. This adjustment aligns the x- and y-axes with the road's width and length, respectively.

Once the orientation is set, noise removal is necessary. Floating points that do not contribute to the accurate representation of the road surface are excluded (such as airborne particles, dust, and rain droplets). These extraneous points, if not removed, can distort measurements and lead to an overestimation of surface defects such as rutting.

4.2. *Pavement Surface Point Cloud Tiling*

Tiling the road surface provides several advantages including: (1) it can help reduce the computational cost by allowing parallel processing, (2) it can facilitate the identification of smaller features in the terrain as the smaller sections make it more convenient to analyze, and (3) it provides an effective method to assess and characterize rutting along the road. For example, tiling the point clouds for separate lanes and specific regions along the longitudinal direction of the pavement provides the ability to analyze certain locations of interest in greater detail. Unlike previous studies, the approach proposed in this paper allows localized pavement assessments by taking the entire 3D feature of each tiled pavement surface instead of assessing the rut depth based on transverse profiles.

Consider a point cloud $P = \{p_1, p_2, \ldots, p_N\}$, where N is the total number of points, and each point $p_i = (x_i, y_i, z_i) \in \mathbb{R}^3$ represents a 3D coordinate in Euclidean space. The road surface is partitioned into tiles by defining boundaries based on the minimum and maximum coordinates in the x, y, and z dimensions. Let T denote the tile size, and let T_x, T_y, and T_z represent the number of tiles in the x, y, and z dimensions, respectively. These are computed as shown in Equation 2:

$$T_x = \left\lceil \frac{\max(x) - \min(x)}{T} \right\rceil, \quad T_y = \left\lceil \frac{\max(y) - \min(y)}{T} \right\rceil, \quad T_z = \left\lceil \frac{\max(z) - \min(z)}{T} \right\rceil,$$

where $\lceil \cdot \rceil$ denotes the ceiling function. The bounds of the (i, j, k)-th tile are then defined as:

$$
\begin{aligned}
x_{\min}^{(i)} &= \min(x) + iT, \quad i = 0, 1, \ldots, T_x - 1, \\
x_{\max}^{(i)} &= x_{\min}^{(i)} + T, \\
y_{\min}^{(j)} &= \min(y) + jT, \quad j = 0, 1, \ldots, T_y - 1, \\
y_{\max}^{(j)} &= y_{\min}^{(j)} + T, \\
z_{\min}^{(k)} &= \min(z) + kT, \quad k = 0, 1, \ldots, T_z - 1, \\
z_{\max}^{(k)} &= z_{\min}^{(k)} + T.
\end{aligned} \tag{2}
$$

The set of points $M_{i,j,k}$ within the (i, j, k)-th tile is given by Equation 3:

$$M_{i,j,k} = \left\{ p_n \in P \mid x_{\min}^{(i)} \leq x_n < x_{\max}^{(i)},\ y_{\min}^{(j)} \leq y_n < y_{\max}^{(j)},\ z_{\min}^{(k)} \leq z_n < z_{\max}^{(k)} \right\}, \tag{3}$$

where $p_n = (x_n, y_n, z_n)$ is the n-th point in the point cloud P. This formulation ensures that each tile contains only the points that lie within its spatial bounds. To improve computational efficiency and focus on meaningful regions, tiles with fewer than a predefined threshold of points are discarded. This step eliminates sparsely populated tiles that may not contribute significantly to the analysis. For this study, the road surface was divided into 1-meter-long strips along the longitudinal direction, with each strip further subdivided into tiles corresponding to individual lanes. This approach ensures a detailed and localized assessment of pavement conditions, particularly in areas prone to rutting.

4.3. *Rut Depth Estimation in Pavement Tiles*

The tiles from a road surface represent the geometry of the undeformed pavement. As the deformations accumulate due to traffic loading, part of the deformation is bounced back due to the viscoelasticity of asphalt, and part is permanently deformed. Therefore, any deviations from the flat surface can indicate the extent of the permanent deformation that occurred in the pavement. To determine the surface depression, a RANdom SAmple Consensus (RANSAC) (Fischler and Bolles 1981). approach can be used to fit each tile to a plane in 3D space since, in any pavement tile, the majority of points are supposed to be flat while rutting includes a relatively less portion of the points. The use of RANSAC in such problems is well-suited since it is ideally suited for applications where interpretation is based on data with typically high error (i.e., a high number of outliers) relative to the optimal feature representation, similar to the case of individual pavement tiles.

Conceptually, RANSAC operates on a simple but powerful principle: it assumes that the data consists of inliers (points that belong to the model, in this case, the flat pavement surface) and outliers (points that do not, such as those in a rut). The algorithm randomly selects a minimal number of points to define a candidate plane and then counts how many other points in the tile fall close to this plane. By repeating this process numerous times, RANSAC identifies the plane supported by the largest consensus of points, effectively isolating the true pavement surface from the rut deformations.

The RANSAC algorithm iteratively determines the best-fit plane for each pavement tile. Inliers are defined as points within a threshold distance of 1 cm from the candidate plane. This threshold is determined based on the precision of the LiDAR sensor and the inherent distribution of the point cloud data.

To obtain the plane, let $\mathcal{P} = \{\mathbf{p}_1, \mathbf{p}_2, \ldots, \mathbf{p}_N\}$ represent a point cloud, where each point $\mathbf{p}_i = (x_i, y_i, z_i) \in \mathbb{R}^3$ corresponds to a 3D coordinate in Euclidean space. The goal is to fit a plane Π to the points in $\mathcal{P}$. A plane in 3D space can be represented by the equation:

$$\Pi : ax + by + cz + d = 0,$$

where $\mathbf{n} = (a, b, c)$ is the unit normal vector to the plane, and d is the perpendicular distance from the origin to the plane. The RANSAC algorithm iteratively estimates the parameters (a, b, c, d) by minimizing the following objective function:

$$\mathcal{L}(\mathbf{n}, d) = \sum_{i=1}^{N} \rho(r_i),$$

where $r_i = |ax_i + by_i + cz_i + d|$ is the residual for the i-th point, and $\rho(\cdot)$ is a loss function that reduces the influence of outliers. For inliers, the residual r_i is within a predefined tolerance ϵ, typically set to 1 cm, which accounts for the accuracy of the LiDAR sensor and the distribution of the point cloud. Once the optimal plane is fitted, the perpendicular distance between the plane and each outlier point is calculated. Specifically, for a given road tile, the lateral deviation below the plane represents the rutting depth. The maximum deviation within the outlier cluster provides the localized rutting depth, while the average lateral distance between the plane and all outlier points quantifies the rutting over the tile. A visual representation of this procedure is illustrated in Figure 7. The figure shows the initial pavement point cloud tile with deformity along the mid-section, the generation of a best-fit plane, and an exaggerated representation of rutting to highlight the lateral distance between the outlier cluster of points and the fitted plane of the pavement surface. Unlike previous studies which rely only on cross-sectional information, our proposed approach takes rutting characterization further because it also accounts for varying rut depth and shapes, and not only a cross-section that may or may not capture the full extent of the rut.

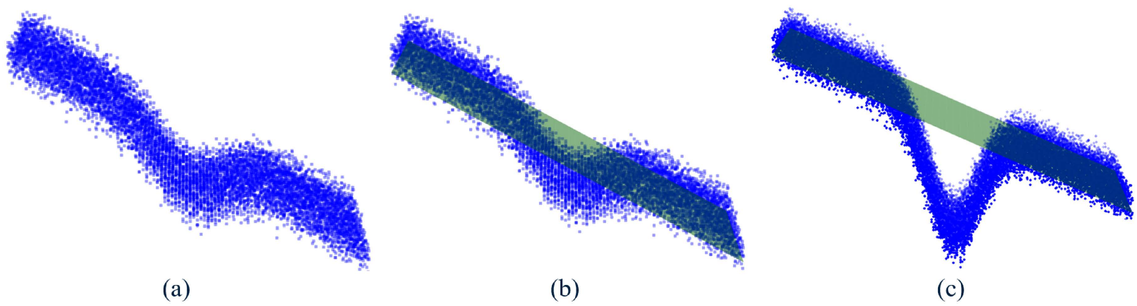

Figure 7.: Visual representation of pavement tile surface fitting: (a) pavement point cloud tile; (b) plane fitting of pavement tile; (c) exaggerated deformed pavement tile.

Once the best-fit plane Π is determined, the perpendicular distance d_i between each outlier point $\mathbf{p}_i$ and the plane is computed as:

$$d_i = \frac{|ax_i + by_i + cz_i + d|}{\sqrt{a^2 + b^2 + c^2}}.$$

For points below the plane, d_i represents the vertical deviation from the plane, which corresponds to the rutting depth. The overall rutting depth for a tile is quantified as the average of the absolute perpendicular distances for all outlier points:

$$\text{Rutting Depth} = \frac{1}{N_{\text{out}}} \sum_{i=1}^{N_{\text{out}}} |d_i|,$$

where N_{out} is the number of outlier points, and d_i is the perpendicular distance for the i-th outlier. This formulation provides a resilient measure of rutting depth by averaging the deviations of the most deformed points from the fitted plane.

5. Results and Discussion

5.1. *Evaluation of Pavement Rutting Using Point Clouds*

To evaluate the performance of the proposed algorithm, five road sections on three highways were selected for testing. Each section represents a different type of highway configuration: (1) TWP510 Road is a three-lane intersection in a relatively rural area and the analysis length was 96 meters, (2) Miette Road is a 130-meter long road segment situated in a narrow mountain landscape, (3) Highway 32 was divided into three segments for analysis where Section 1 is a two-lane undivided highway spanning 181 meters; Section 2 is a three-lane undivided highway with a length of 96 meters; and Section 3 is a 62-meter-long three-lane undivided highway featuring a left-turn lane at a signalized intersection.

The road sections were selected to represent different lane functions as the traffic type, loading, and volume typically vary for each lane, and consequently, so would the strains and stresses imposed on the pavement. The rut depths varied between 3.42 mm and 43.21 mm across the road segments as shown in Figure 8. The kernel density method in the violin plot represents the distribution of the average rutting measurements in each tested road section. The mean rut depth refers to the average of the rut measurements in each lane. Each tick represents one rut value in a 1-meter strip tile along the road's longitudinal length and the distribution of the rutting measurements demonstrates the degree of rutting for each segment and whether any extreme values are present.

Among the assessed road sections, TWP510 Road exhibited the most favorable rut performance, demonstrating the least deformation in terms of average rut depth across both lanes. It is worth noting that TWP 510 had recently undergone resurfacing when the scan data was collected. Following TWP510, Miette Road and Highway 32 Section 1 also showed relatively low rut depths. However, in contrast, Highway 32 Section 3 displayed the poorest rut performance, characterized by the highest average rut depths across both lanes. It is worth noting that Highway 32 section 3 also exhibited anomalous measurements, further emphasizing its deteriorated condition compared to the other road sections due to the potential presence of potholes or severely chipped aggregates from the pavement surface.

These quantitative results are directly relevant to pavement management practices, where specific rut depth thresholds trigger maintenance actions. In Canada, many transportation agencies, often following guidelines from the Transportation Association of Canada (TAC) or province-specific specifications, use a tiered approach for intervention. Rut depths approaching 10–15 mm are typically considered a threshold for concern, prompting further monitoring as they can increase hydroplaning risk. Depths exceeding 20–25 mm are generally classified as severe and often warrant corrective action, such as milling and overlay, to restore pavement safety and functionality (Chen *et al.* 2020). Therefore, the measurements on Highway 32 Section 3, which frequently exceed 20 mm and reach a maximum of 43.21 mm, would signal a clear need for urgent rehabilitation under these standards. In contrast, the shallower ruts on TWP510 and Miette Road would likely fall into a routine monitoring category, which points to the algorithm's capability to differentiate between pavement sections requiring immediate attention and those in acceptable condition.

The calculated rut depths for each road section across each lane are summarized in Figure 9.

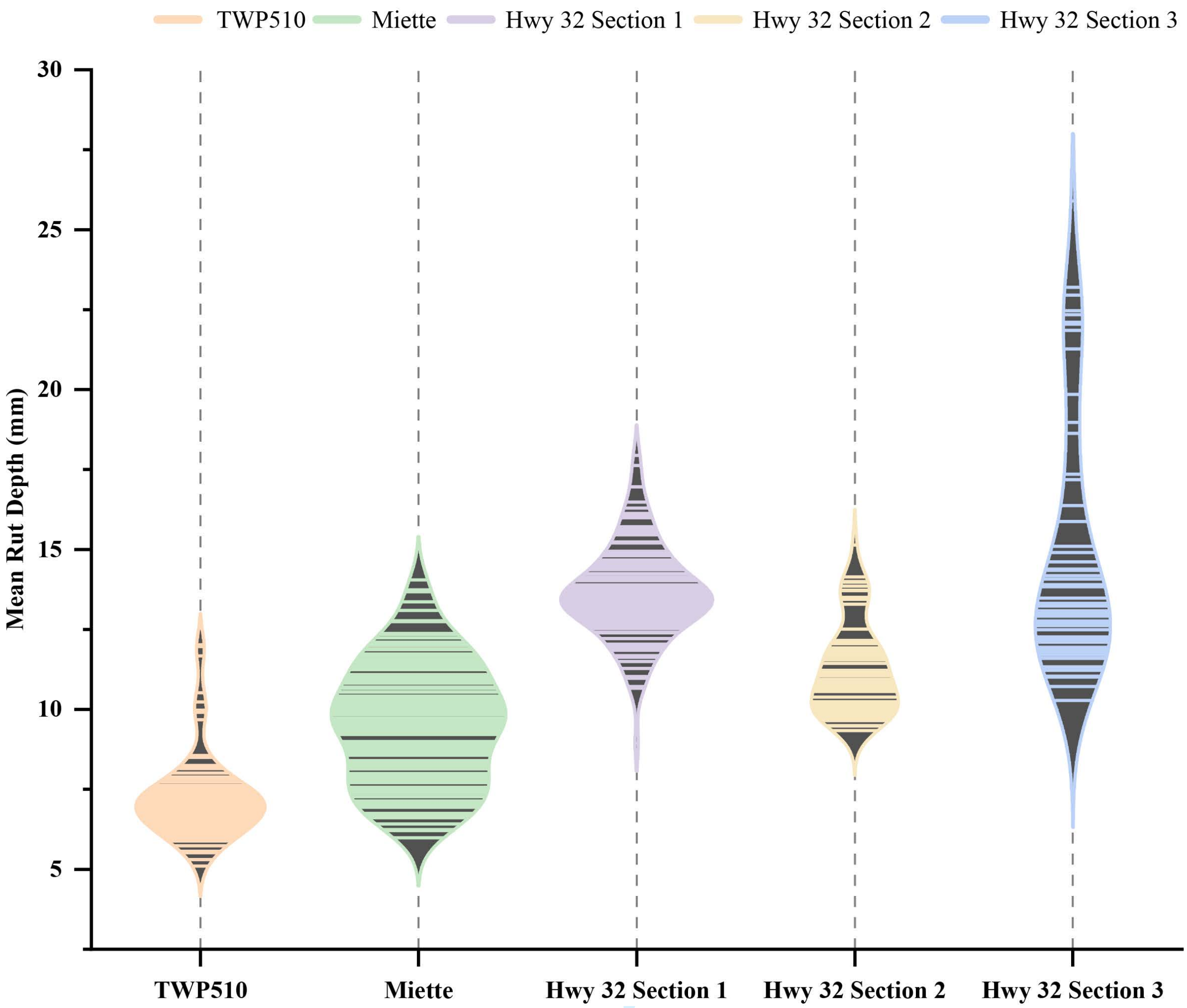

Figure 8.: Violin plot showing the distribution of average rutting measurements in each tested road section.

Mobile LiDAR technology was used to create a highly accurate 3D representation of the road environment with a relative accuracy of 1 mm. This highly detailed digital twin facilitates the detection of subtle deformations in the road surface. Similar to field measurements where rutting is quantified as depressions in the road surface along the wheel path (FHWA 2014), the method proposed in this paper involves measuring the depth of deformation across pavement tiles and mapping these sequentially along the road to detect rutting patterns, which typically appear as consistent, longitudinal depressions along wheel paths. Consistent, longitudinal depressions are indicative of rutting, whereas abrupt depth changes often suggest other failures like potholes. The heatmap visualization in Figure 9 distinguishes between consistent rutting patterns and areas where measurements indicate multiple types of pavement failures.

Within TWP510 Road, a problematic region was identified at the end of the middle lane. While Miette Road had lesser ruts in the right lane, the left lane had several regions of deteriorated pavement condition (Figure 9b) due to the presence of cracks upon visual inspections. Similarly, on Highway 32, several localized rutting areas are observed across the three road segments. The rutting measurements were similar between Highway 32 Sections 1 and 2, where some regions are affected by 20 mm ruts along the right lane.

Particularly noteworthy are the excessive deformation depths measured as shown in Figure 9e which suggests the presence of underlying pavement failures, besides rutting, in the queue box area at the end of the road segment. Further investigation would be necessary to determine the cause of the abnormal rut measurements detected in these tile segments. A transversal profile

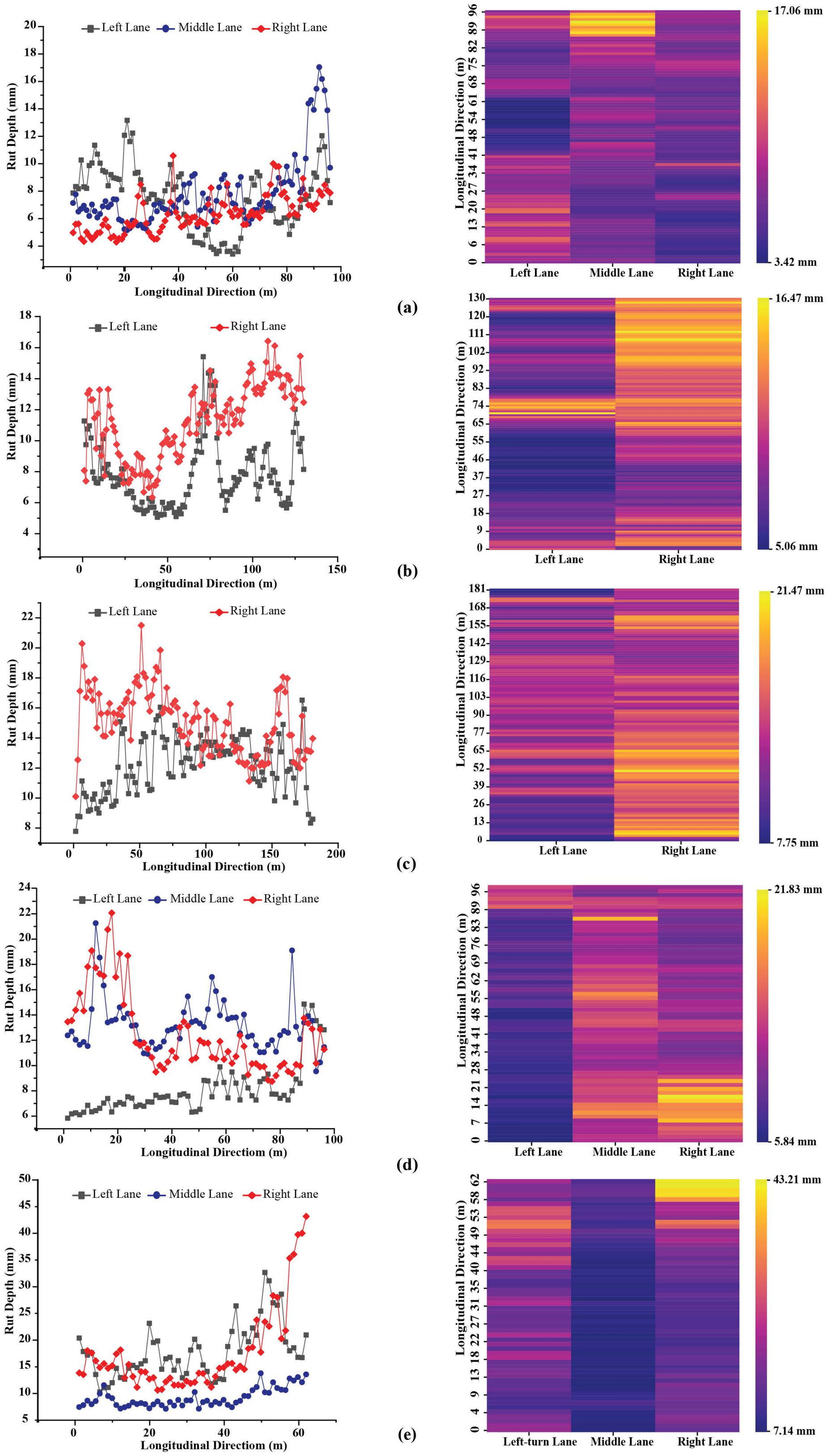

Figure 9.: Rutting depths along the longitudinal direction supplemented by a heatmap. (a) TWP510 Road;(b) Miette Road; (c) Highway 32 – 1; (d) Highway 32 – 2; (e) Highway 32 – 3.

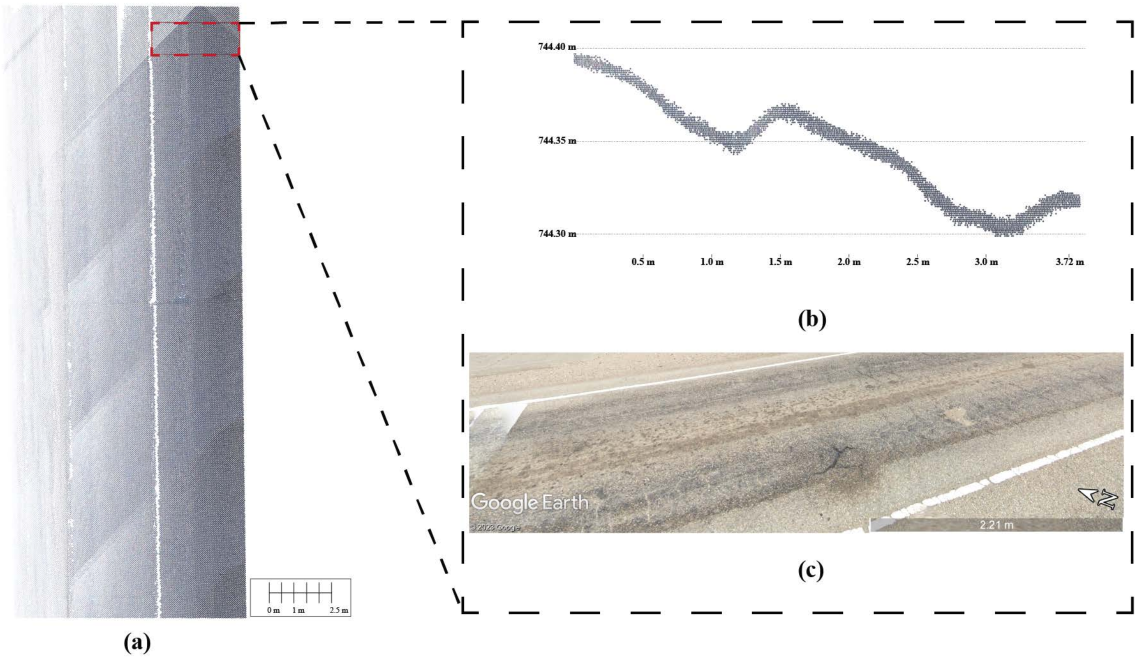

Figure 10.: Examination of a sample region flagged by the algorithm (Highway 32 – 3). (a) point cloud; (b) a transversal profile showing the deformation along the wheel path; (c) a satellite image of the location with several failure mechanisms (Google 2023).

analysis of the area can provide valuable insights into the nature of the deformation.

Before examining the profile, it is important to note that the scope of this study is not to imply causation in presenting the results but rather to provide insightful information regarding pavement condition evaluation to aid in timely maintenance operations. As illustrated in Figure 10, the examination of the transversal profile at the queue box reveals two key observations: (1) the rutting extent illustrated in the profile in Figure 10b corresponds well with the proposed methodology, validating its efficacy in identifying both the magnitude and spatial information of rutting within each 3D tile. This substantiates the algorithm's consistency in assessing the rut severity. (2) Visual inspections conducted at the identified location indicate that the pavement condition in this region is aggravated by concurrent pavement failure mechanisms. In such instances, the algorithm indirectly identifies locations where the pavement has experienced substantial deterioration, as evident by the presence of various distress types, including potholes, alligator and thermal cracks, aggregate raveling, and elevated rutting along the wheel path (see Figure 10c).

In addition, the proposed algorithm was capable of highlighting the different rutting severities across different test sections with different road conditions. For example, TWP510 serves as a typical example of a rural highway configuration in a less congested rural area. The reduced cumulative stress exerted on the pavement by lower traffic volumes results in less significant pavement deformations. Moreover, the recent asphalt resurfacing prior to data collection might have restored the structural integrity of the pavement surface. Situated in a mountainous region in the province of Alberta, Miette Road presents a narrow and less traveled route, primarily due to its closure between November and April due to harsh climatic conditions. This road also faces restrictions on vehicle types throughout the year. The relatively shallow rut depths observed, with a maximum of 16.47 mm, indicate that the pavement structure is designed to withstand temperature-induced stresses, and a lighter traffic-related pavement fatigue. Highway 32 is located in a highly trafficked urban area. Higher overall rutting depths were recorded for all three sections, with a maximum of 21.47 mm, 21.83 mm, and 43.21 mm for Section 1, 2, and 3, respectively. This can be attributed to the increased traffic capacity and the presence of intersections that increase the imposed stresses on the pavement infrastructure.

Pavement deterioration is a multifaceted process that arises from various factors rather than a single cause, resulting from the interaction of vehicle-related and environmental influences, along with multiple simultaneous distresses. For example, the durability of the pavement significantly relies on the initial construction phases, such as the compaction process, which must be executed properly to ensure that the pavement can support the weight of vehicles without significant consolidation or deformation under service conditions (Xing *et al.* 2024).

Furthermore, if the asphalt mix design was subpar, it could also play a role in the deterioration. The constant stress from heavy vehicles like trucks and buses, along with extended loading durations, can lead to issues such as ruts, potholes, and cracks. This is particularly noticeable when numerous factors related to the asphalt mix design and road structure contribute to accelerated pavement wear due to traffic types and loads not anticipated during the initial planning phases (Xing *et al.* 2024).

In addition, environmental elements such as temperature changes can result in the materials expanding and contracting over repeated cycles, eventually causing cracking, especially if the materials were not designed to accommodate such temperature shifts. For instance, Edmonton, Alberta experiences temperature variations ranging from a high of 37.2 degrees Celsius in the height of summer to a low of -40 degrees during the coldest winter days. Other environmental conditions, such as rainfall, can worsen pavement distress by allowing water to infiltrate existing cracks. This situation, combined with freeze-thaw cycles, can lead to larger or new cracks that ultimately compromise the road's structural integrity. These processes are recognized as contributing factors to the degradation of flexible pavement in particular (Piryonesi and El-Diraby 2021). Identifying these types of distresses and their coexistence within the studied area not only highlights the complexity of pavement degradation but also emphasizes the necessity for thorough assessment and condition evaluation techniques.

5.2. *Effects of Point Density on Rutting Assessment*

To assess the variation in rutting measurements, the algorithm was repeatedly applied to the Highway 32 LiDAR dataset with a reduced point density. This reduced dataset, known as the "thinned version," reflects a 75% reduction in point density, as detailed in section 3.2.1. Figure 11 illustrates the rut depths recorded along the longitudinal direction of Highway 32. Each segment of 113 meters corresponds to a lane: the first 113 meters represent the left lane, while the subsequent section corresponds to the right lane. In summary, as observed in Figure 11, at moderate reduction levels (1163.45 - 233.72 *ppsm*), the general trend of rut depth remains well preserved, though some finer details are lost. The rut depths still retain all key trends, with rutting measurements varying between 0-2 mm. However, as density reductions increase to 90% (a *ppsm* of 125.11), rutting measurements deviate from those recorded at "ground truth" high-resolutions, especially measurements of the peaks and dips, reaching a maximum deviation of 4 mm.

The results presented in Table 2 highlight the relationship between point density and rut depth variations measured at 50-meter intervals. The first row under the headers represents the estimated *ppsm* values for each reduction level, showing how the density of data points decreases progressively.

As observed, moderate reductions in point density (10% to 75%) lead to relatively minor deviations in rut depth measurements, with differences hovering around an average of 2.5 mm across all intervals. This suggests that these reductions retain the fundamental characteristics of the rut profile while slightly smoothing out minor variations, yet still maintain a reliable representation of rut depth trends.

However, at higher reduction levels (90%), where point densities drop to 125.11 *ppsm*, the deviation becomes significantly more pronounced, with differences exceeding 3 mm to 5 mm. The loss of finer point details at these levels results in noticeable distortions, particularly in capturing peak and dip variations. These findings align with Figure 11, where lower-density datasets struggle to accurately preserve local rut depth fluctuations.

Overall, while a moderate reduction in point density may provide computational efficiency

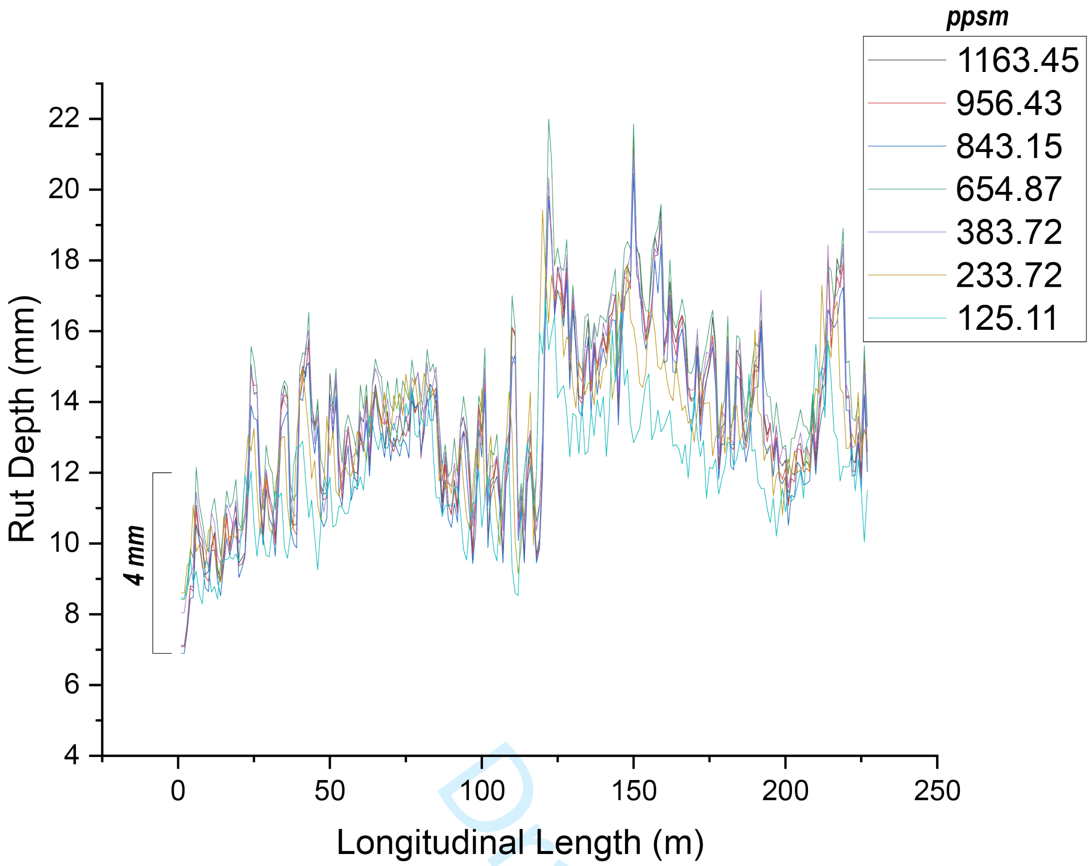

Figure 11.: Measurement deviation across different point density reduction levels.

Table 2.: Average rut depth differences at 50m intervals along the longitudinal direction

Interval (m)	**Difference in Rut Depth (mm)**						
	High Res	10%	25%	33%	50%	75%	90%
ppsm	1280	1163.45	956.43	843.15	654.87	233.72	125.11
0	11.29	0.13	0.52	0.85	1.25	2.21	3.88
50	12.99	0.18	0.49	0.80	1.20	2.19	3.69
100	14.54	0.17	0.45	0.78	1.31	2.49	4.25
150	15.21	0.24	0.64	0.96	1.53	2.88	5.41
200	13.91	0.21	0.63	0.79	1.35	2.21	4.10

Note: The first row under the headers represents the estimated *ppsm* values corresponding to each reduction level. The remaining rows display the average differences in rut depth (mm) compared to high-resolution data.

without major accuracy loss, extreme reductions (above 75%) lead to data degradation, potentially affecting the reliability of rut depth assessments. Consequently, selecting an optimal density threshold is crucial for balancing data efficiency with measurement accuracy.

Statistical Framework for Method Comparison

One of the key challenges in evaluating LiDAR-based rut depth measurements is balancing statistical significance with practical relevance. Let $D_0 = \{d_{0,i}\}_{i=1}^{M}$ be the set of rut depth measurements from the high-resolution reference dataset (with density ρ_0) and let $D_k = \{d_{k,i}\}_{i=1}^{M}$ be the measurements from a dataset with a reduced point density $\rho_k < \rho_0$.

Traditional hypothesis tests, such as a paired t-test, would evaluate the null hypothesis $H_0 : \mu_d = 0$, where μ_d is the mean of the differences $d_{0,i} - d_{k,i}$. With large sample sizes typical of LiDAR data, even minute, practically irrelevant differences can yield a statistically significant result (i.e., a very small p-value), leading to the rejection of H_0. This highlights the classic issue where statistical significance does not equate to practical importance.

In contrast, the Bland-Altman method provides a more intuitive and application-oriented approach. It quantifies the agreement between two measurement techniques by analyzing the distribution of their differences. For each corresponding pair of measurements $(d_{0,i}, d_{k,i})$, we compute the mean and the difference:

$$\text{Mean measurement:} \quad m_i = \frac{d_{0,i} + d_{k,i}}{2}$$
$$\text{Difference:} \quad \delta_i = d_{0,i} - d_{k,i}$$

The analysis then focuses on the statistical properties of the differences δ_i. The key metrics are the mean bias $(\bar{\delta})$ and the standard deviation of the differences (σ_δ):

$$\bar{\delta} = \frac{1}{M}\sum_{i=1}^{M}\delta_i, \qquad \sigma_\delta = \sqrt{\frac{1}{M-1}\sum_{i=1}^{M}(\delta_i - \bar{\delta})^2}.$$

The 95% limits of agreement (LoA) are then defined as:

$$\text{LoA} = \bar{\delta} \pm 1.96\,\sigma_\delta.$$

This interval, $[\bar{\delta} - 1.96\sigma_\delta, \bar{\delta} + 1.96\sigma_\delta]$, provides an estimate for the range within which 95% of the differences between the two methods are expected to fall.

In each plot in Figure 12, the x-axis represents the mean rut depth m_i, while the y-axis shows the difference δ_i. The central solid line represents the mean bias $\bar{\delta}$, and the dashed blue lines denote the limits of agreement. These limits illustrate the extent to which individual measurements deviate from the high-resolution reference and provide a clearer picture of measurement reliability from a practical standpoint.

For example, at a 10% reduction in point density, the mean bias was $\bar{\delta} = 0.187$ mm, with limits of agreement $[-0.255$ mm, 0.629 mm$]$. The clustering of data points around the zero-difference line suggests that the reduction introduces minimal systematic error. As the reduction increased to 75%, the mean bias rose to $\bar{\delta} = 2.315$ mm, with LoA of $[-0.157$ mm, 4.889 mm$]$, indicating a notable increase in both systematic bias and random error (dispersion). The highest reduction level of 90% resulted in a mean bias of $\bar{\delta} = 4.376$ mm, with LoA spanning $[0.420$ mm, 8.333 mm$]$, reflecting a significant loss of measurement reliability.

The Bland-Altman analysis reveals that reductions up to 75% (corresponding to $\rho_k \approx 233$ *ppsm*) maintain a level of agreement that may be acceptable for practical applications. Beyond this threshold, the deviations become too large. This leads to the formulation of a practical acceptance criterion. According to the FHWA, which uses AASHTO standard R 88-18:2018 (AASHTO 2018), a profiler's accuracy should be within ±2 mm of a manual survey. We can therefore define

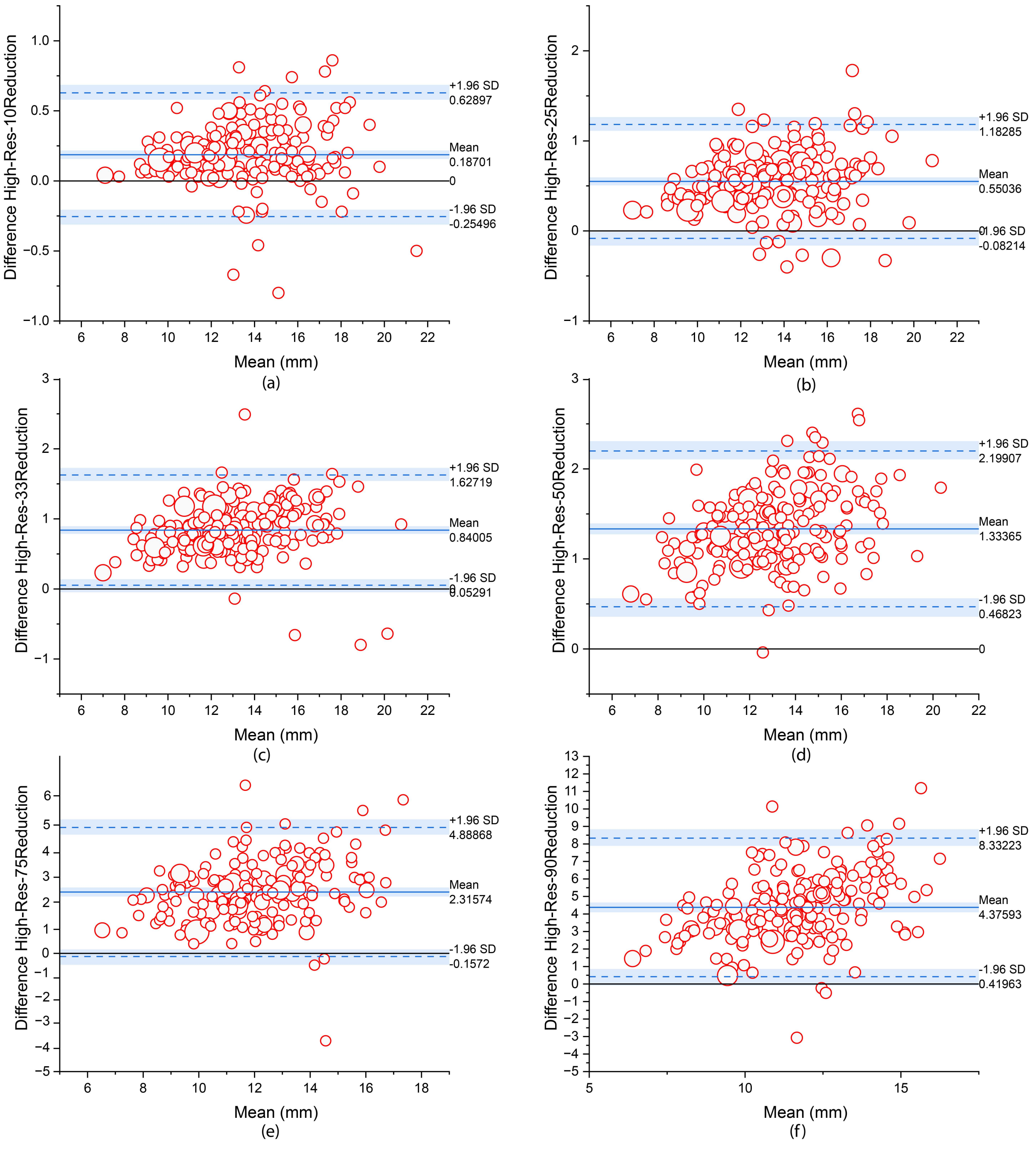

Figure 12.: Bland-Altman plots comparing rut depth measurements from high-resolution LiDAR data with progressively reduced point density datasets. Each subplot represents a different level of point density reduction: (a) 1280 *ppsm* vs. 1163.45 *ppsm*, (b) 1280 *ppsm* vs. 956.43 *ppsm*, (c) 1280 *ppsm* vs. 843.15 *ppsm*, (d) 1280 *ppsm* vs. 654.87 *ppsm*, (e) 1280 *ppsm* vs. 233.72 *ppsm*, (f) 1280 *ppsm* vs. 125.11 *ppsm*.

an acceptable deviation threshold, $T_{\text{accept}} = 2$ mm. A reduced-density measurement method is considered reliable if its measurement uncertainty falls within this tolerance. Based on our analysis, a point density of $\rho_{\min} \approx 230$ *ppsm* represents a viable lower-bound threshold, as the bias and variability at this level remain within the ≈ 2 mm engineering tolerance, thus ensuring accurate rut depth assessments while maximizing cost and computational efficiency.

5.3. *Practical Utility and Deployment Considerations*

In practical deployment scenarios-particularly on busy urban corridors and multi-lane highways—the method's ability to collect high-resolution LiDAR data at normal traffic speeds must be complemented by strategies that facilitate near real-time performance and computational efficiency. The pavement surface is initially segmented using deep learning techniques. Segmentation models, such as KPConv (Thomas *et al.* 2019), are trained on labeled point clouds where each point is preclassified into categories (roads, buildings, vegetation, traffic signs, etc.). The network learns to predict these categories by minimizing the discrepancy or error between its predictions and the actual labels during training. During inference, the model can process unseen point cloud data from scans to segment and classify each point based on the learned model. These methods effectively isolate road features from surrounding objects, even in environments crowded with vehicles and highway infrastructure, resulting in an isolated pavement surface that can be efficiently analyzed. While this process requires higher computational power, it remains significantly lower than image or vision-based techniques. This step not only enhances data quality by removing extraneous elements but also streamlines subsequent processing.

In the proposed computational experiments, the algorithm demonstrated a runtime of approximately 83 seconds when processing 24 million points corresponding to 561 meters of pavement (equivalent to about 147 seconds per kilometer). This overall runtime encompasses the entire workflow—including the tiling of the pavement surface, and iterative RANSAC-based measurement of rut depths for each tile. The runtime is significantly lowered to 34 seconds per kilometer at a *ppsm*of 230. These performance levels were attained by leveraging a multi-core architecture on a PC equipped with a 12th-generation Intel i7-12700k processor (12 cores and 20 threads). The algorithm demonstrated high efficiency, maintaining a modest memory footprint (approximately 5.1 GB of 64 GB available) and scaling well to large datasets. The design choices outlined highlight the method's potential for evaluating pavement at the network level. This approach integrates deep learning to accurately segment road surfaces and utilizes an efficient, scalable computational framework, making it suitable for near real-time applications. It enables transportation agencies to proactively monitor and maintain roadway infrastructure in near real-time while operating seamlessly alongside regular traffic, without requiring stops or interruptions during data collection.

It is also important to contrast the proposed 3D LiDAR approach with existing cost-effective technologies, such as dedicated laser profilers. While laser profilers are effective for measuring transverse profiles, they are inherently limited to scanning a single lane across the pavement, which necessitates performing multiple passes across the road to capture permanent deformations across all lanes. In contrast, the proposed method using LiDAR in this study analyzes the full 3D surface geometry, providing a more comprehensive and spatially aware assessment of pavement deformation. Furthermore, the value of mobile LiDAR extends far beyond rutting. The same dataset collected in a single pass at highway speeds can be repurposed for a wide range of pavement and asset management tasks, including pothole detection, crack mapping, traffic sign inventory, and clearance measurements. This multi-function capability presents a significant advantage in terms of operational efficiency and long-term return on investment compared to single-purpose technologies for approximately the same cost or even less when compared to more advanced laser scanners.

However, it is important to acknowledge potential limitations in certain operational environments. In heavy traffic, vehicle occlusion can create gaps or "shadows" in the pavement data. While the deep learning-based segmentation effectively filters out points from other vehicles, severe occlusion may lead to insufficient data density in some tiles, potentially impacting the reliability of rut measurements. To mitigate this, data collection during off-peak hours is recommended for heavily congested corridors.

Furthermore, adverse weather presents a significant challenge. Rain can lead to standing water that obscures the true pavement surface, causing underestimation of rut depths, while snow cover can render data collection infeasible.

It is important, however, to contextualize these challenges. As an active sensing technology, LiDAR is inherently immune to ambient lighting conditions and shadows, which are significant sources of error for passive, image-based systems. While heavy rain and occlusion remain shared challenges, LiDAR's direct 3D data acquisition and robustness to lighting variations make its operational constraints generally less severe than those faced by stereo-vision techniques.

6. Conclusion and Summary

This paper introduced a novel and highly efficient method for the automated assessment of pavement rutting using high-resolution 3D LiDAR data. The proposed algorithm demonstrates exceptional accuracy, successfully capturing shallow rut depths as low as 3 mm and reliably distinguishing between rutting severities across different road sections. By directly processing the 3D point cloud, the method avoids computationally expensive rendering of 2D images and provides robust measurements consistent with field observations, as validated through ad hoc profile analysis. The algorithm's performance, achieving rutting estimation at a rate of approximately 147 seconds per kilometer (or 34 seconds per kilometer for low-cost LiDAR with lower *ppsm*), highlights its suitability for large-scale, network-level deployment.

A central contribution of this work is the systematic evaluation of the impact of point cloud density on measurement accuracy. Through a Bland-Altman analysis, this study quantified the trade-off between data resolution and measurement reliability, revealing that extreme reductions (above 75%) lead to unreliable assessments. Specifically, this study establishes a practical lower-bound threshold of approximately 230 ppsm. This finding has direct implications for pavement management, demonstrating that agencies can deploy more affordable LiDAR sensors for large-scale, network-level surveys. By doing so, they can optimize operational costs without compromising the integrity of maintenance and rehabilitation decisions or the stringent ± 2 mm accuracy requirements common in engineering practice. This work, therefore, provides a clear, data-driven framework for integrating advanced remote sensing into proactive infrastructure monitoring in a targeted and cost-effective manner.

Future work will focus on developing a predictive model to formally characterize the relationship between point density and measurement error. Such a model would enable a more dynamic, risk-based approach to data processing. Furthermore, the core methodology can be extended to assess other critical pavement distresses, such as potholes. A key objective will be to determine the minimum point density thresholds required for their reliable detection and quantification, particularly with more accessible, lower-cost LiDAR systems, thereby creating a more comprehensive and cost-effective pavement assessment platform.

Data Availability

LiDAR datasets used during the study are proprietary and confidential in nature. Specific queries regarding data access and potential availability can be directed to the corresponding author.

Acknowledgement

The authors would like to acknowledge Nektar3D for providing the LiDAR datasets from Alberta for this study. This research has received funding through the NSERC Alliance Mitacs Accelerate

Grant.

Competing interests

The authors declare there are no competing interests.

References

AASHTO, 2018. *Standard Practice for Collecting the Transverse Pavement Profile*. American Association of State Highway and Transportation Officials, Standard R 88-18. Available from: https://www.transportation.org/aashto-publications/.

Arezoumand, S., *et al.*, 2021. Automatic pavement rutting measurement by fusing a high speed-shot camera and a linear laser. *Construction and Building Materials*, 283, 122668.

ASTM, 2023. *Test method for measuring rut-depth of pavement surfaces using a straightedge*. ASTM International. Report No. E1703/E1703M.

Boulch, A., 2020. Convpoint: Continuous convolutions for point cloud processing. Available from: https://arxiv.org/abs/1904.02375.

Cao, M.T., *et al.*, 2021. Image processing-based automatic detection of asphalt pavement rutting using a novel metaheuristic optimized machine learning approach. *Soft Computing*, 25 (20), 12839–12855.

Chen, L., *et al.*, 2020. Determination of Allowable Rutting Depth Based on Driving Safety Analysis. *Journal of Transportation Engineering, Part B: Pavements*, 146 (2), 04020023.

Chilukwa, N. and Lungu, R., 2019. Determination of Layers Responsible for Rutting Failure in a Pavement Structure. *Infrastructures*, 4 (2), 29.

Dhiman, A. and Klette, R., 2020. Pothole Detection Using Computer Vision and Learning. *IEEE Transactions on Intelligent Transportation Systems*, 21 (8), 3536–3550.

El Issaoui, A., *et al.*, 2021. Feasibility of Mobile Laser Scanning towards Operational Accurate Road Rut Depth Measurements. *Sensors*, 21 (4), 1180.

Esri, 2023. *Light gray canvas [basemap]. scanned locations using the Leica Pegasus Two Ultimate scanning system* [Available online]. Available from: https://www.arcgis.com/home/item.html?id=33ea4550c8144e66847d902e4766c2f7.

Faisal, A. and Gargoum, S., 2023-12-03. Automated Assessment of Pavement Rutting Using Mobile LiDAR Data. Available from: https://trid.trb.org/View/2301594.

Faisal, A. and Gargoum, S., 2025a. Cost-effective lidar for pothole detection and quantification using a low-point-density approach. *Automation in Construction*, 172, 106006. Available from: https://www.sciencedirect.com/science/article/pii/S0926580525000469.

Faisal, A. and Gargoum, S., 2025b. Tile-based pavement rutting and roughness evaluation using mobile lidar data. *Journal of Transportation Engineering, Part B: Pavements*, 151 (3), 04025033. Available from: https://ascelibrary.org/doi/abs/10.1061/JPEODX.PVENG-1573.

Famili, A., *et al.*, 2021. Application of Mobile Terrestrial LiDAR Scanning Systems for Identification of Potential Pavement Rutting Locations. *Transportation Research Record*, 2675 (9), 1063–1075.

Fan, R., *et al.*, 2020. Pothole Detection Based on Disparity Transformation and Road Surface Modeling. *IEEE Transactions on Image Processing*, 29, 897–908.

Feng, H., *et al.*, 2022. GCN-Based Pavement Crack Detection Using Mobile LiDAR Point Clouds. *IEEE Transactions on Intelligent Transportation Systems*, 23 (8), 11052–11061.

FHWA, 2014. *Distress identification manual for the ltpp program*. Federal Highway Administration. Report No. FHWA-HRT-13-092.

Firoozi Yeganeh, S., Golroo, A., and Jahanshahi, M.R., 2019. Automated Rutting Measurement Using an Inexpensive RGB-D Sensor Fusion Approach. *Journal of Transportation Engineering, Part B: Pavements*, 145 (1), 04018061.

Fischler, M.A. and Bolles, R.C., 1981. Random Sample Consensus: A Paradigm for Model Fitting with Apphcatlons to Image Analysis and Automated Cartography. *Communications of the ACM*, 24 (6).

Fwa, T.F., Pasindu, H.R., and Ong, G.P., 2012. Critical Rut Depth for Pavement Maintenance Based on Vehicle Skidding and Hydroplaning Consideration. *Journal of Transportation Engineering*, 138 (4), 423–429.

Gargoum, S. and Gargoum, S., 2024. Automatically Refining Degraded and Occluded Lane Marking

Information to Enhance the quality of High Definition Maps for Autonomous Vehicles. *Transportation Research Record*, 2678 (3), 37–49.

Gargoum, S. and El-Basyouny, K., 2017. Automated extraction of road features using LiDAR data: A review of LiDAR applications in transportation. *In*: *2017 4th International Conference on Transportation Information and Safety (ICTIS)*, August, Banff, AB, Canada. IEEE, 563–574.

Gargoum, S., *et al.*, 2017. Automated Highway Sign Extraction Using Lidar Data. *Transportation Research Record: Journal of the Transportation Research Board*, 2643 (1), 1–8.

Gargoum, S.A., *et al.*, 2018a. A Fully Automated Approach to Extract and Assess Road Cross Sections From Mobile LiDAR Data. *IEEE Transactions on Intelligent Transportation Systems*, 19 (11), 3507–3516.

Gargoum, S.A., El-Basyouny, K., and Sabbagh, J., 2018b. Assessing Stopping and Passing Sight Distance on Highways Using Mobile LiDAR Data. *Journal of Computing in Civil Engineering*, 32 (4), 04018025.

Gézero, L. and Antunes, C., 2019. Road Rutting Measurement Using Mobile LiDAR Systems Point Cloud. *ISPRS International Journal of Geo-Information*, 8 (9), 404.

Ghosh, R. and Smadi, O., 2021. Automated Detection and Classification of Pavement Distresses using 3D Pavement Surface Images and Deep Learning. *Transportation Research Record*, 2675 (9), 1359–1374.

Google, 2023. *Google Maps location showing the pavement condition at queue box*. Available from: https://goo.gl/maps/bbeZft1r2pp4Ujmr6.

Gouda, M., *et al.*, 2023. Traffic sign extraction using deep hierarchical feature learning and mobile light detection and ranging (LiDAR) data on rural highways. *Journal of Intelligent Transportation Systems*, 27 (5), 643–664.

Guan, H., *et al.*, 2015. Iterative Tensor Voting for Pavement Crack Extraction Using Mobile Laser Scanning Data. *IEEE Transactions on Geoscience and Remote Sensing*, 53 (3), 1527–1537.

Hatoum, M.B., *et al.*, 2023. Wireless and Sensing Technologies in US Highway Projects: Usage, Maturity, Challenges, and KPIs. *In*: *International Conference on Transportation and Development 2023*, June, Austin, Texas. American Society of Civil Engineers, 501–511.

Ji, X., *et al.*, 2016. Development of a rutting prediction model for asphalt pavements with the use of an accelerated loading facility. *Road Materials and Pavement Design*, 17 (1), 15–31.

Jung, J. and Bae, S.H., 2018. Real-Time Road Lane Detection in Urban Areas Using LiDAR Data. *Electronics*, 7 (11), 276.

Li, Y., *et al.*, 2018. Pointcnn: Convolution on $\mathcal{X}$-transformed points. Available from: https://arxiv.org/abs/1801.07791.

Liu, R., *et al.*, 2022. 3D Rutting Features Extraction Through Continuous Pavement Laser Point Cloud. *International Journal of Pavement Research and Technology*.

Ma, L. and Li, J., 2022. SD-GCN: Saliency-based dilated graph convolution network for pavement crack extraction from 3D point clouds. *International Journal of Applied Earth Observation and Geoinformation*, 111, 102836.

Phan, A.T.T. and Huynh, T.N., 2022. Pavement Crack Extraction Method from Mobile Laser Scanning Point Cloud. *Advances in Civil Engineering*, 2022, 1–11.

Piryonesi, S.M. and El-Diraby, T., 2021. Climate change impact on infrastructure: A machine learning solution for predicting pavement condition index. *Construction and Building Materials*, 306, 124905.

Qi, C.R., *et al.*, 2017. Pointnet++: Deep hierarchical feature learning on point sets in a metric space.

Saha, P.K., *et al.*, 2022. Road Rutting Detection using Deep Learning on Images. *In*: *2022 IEEE International Conference on Big Data (Big Data)*, December. 6507–6515.

Serigos, P.A., *et al.*, 2012. Field Evaluation of Automated Rutting Measuring Equipment. *No. FHWA/TX-12/0-6663-1 Center for Transportation Research, The University of Texas, Austin.*

Shahrestani, A., Faisal, A., and Gargoum, S., 2024. Pavement Crack Image Generation and Data Balancing Using Deep Adversarial Generative Networks. Available from: https://trid.trb.org/View/2444811.

Shatnawi, N., Obaidat, M.T., and Al-Mistarehi, B., 2021. Road pavement rut detection using mobile and static terrestrial laser scanning. *Applied Geomatics*, 13 (4), 901–911.

Shatnawi, N., Taleb Obaidat, M., and Al-Sharideah, A., 2022. Modeling Road Pavement Rutting Using Artificial Neural Network and Conventional Measurements. *Transportation Research Record: Journal of the Transportation Research Board*, 036119812211102.

Shtayat, A., *et al.*, 2020. A review of monitoring systems of pavement condition in paved and unpaved roads. *Journal of Traffic and Transportation Engineering (English Edition)*, 7 (5), 629–638.

Singh, A.K. and Sahoo, J.P., 2021. Rutting prediction models for flexible pavement structures: A review of historical and recent developments. *Journal of Traffic and Transportation Engineering (English*

Edition), 8 (3), 315–338.
Tamagusko, T., Gomes Correia, M., and Ferreira, A., 2024. Machine learning applications in road pavement management: A review, challenges and future directions. *Infrastructures*, 9 (12).
Thomas, H., *et al.*, 2019. KPConv: Flexible and Deformable Convolution for Point Clouds. *In*: *2019 IEEE/CVF International Conference on Computer Vision (ICCV)*, October, Seoul, Korea (South). IEEE, 6410–6419. Available from: https://ieeexplore.ieee.org/document/9010002/.
Tripathi, A., *et al.*, 2023. People, Process, and Technology Maturity Levels for Successful Technology Implementation by State Departments of Transportation. *Transportation Research Record: Journal of the Transportation Research Board*, 036119812311700.
Wang, K.C.P. and Smadi, O., 2011. *Transportation Research Circular E-C156: Automated Imaging Technologies for Pavement Distress Surveys*. Washington, D.C.: Transportation Research Board.
Xing, M., *et al.*, 2024. Investigation of the properties of high-viscosity modified asphalt binder under hygrothermal environments. *Materials*, 17 (12), 2869.
Xu, X. and Yang, H., 2019. Intelligent crack extraction and analysis for tunnel structures with terrestrial laser scanning measurement. *Advances in Mechanical Engineering*, 11 (9), 168781401987265.
Xu, Y., *et al.*, 2023. VIDAR-Based Road-Surface-Pothole-Detection Method. *Sensors (Basel, Switzerland)*, 23 (17), 7468.
Yongtao Yu, *et al.*, 2014. 3D crack skeleton extraction from mobile LiDAR point clouds. *In*: *2014 IEEE Geoscience and Remote Sensing Symposium*, July, Quebec City, QC. IEEE, 914–917.
Zhong, M., *et al.*, 2020. Pavement Crack Detection from Mobile Laser Scanning Point Clouds Using a Time Grid. *Sensors*, 20 (15), 4198.
Zhu, W., *et al.*, 2021. A capsnets approach to pavement crack detection using mobile laser scannning point clouds. *The International Archives of the Photogrammetry, Remote Sensing and Spatial Information Sciences*, XLIII-B1-2021, 39–44.